

The SkyMapper Transient Survey

R. A. Scalzo^{1,2,3,6}, F. Yuan^{1,2}, M. J. Childress^{1,2,4}, A. Möller^{1,2}, B. P. Schmidt^{1,2}, B. E. Tucker^{1,2},
 B. R. Zhang^{1,2}, C. A. Onken^{1,2}, C. Wolf^{1,2}, P. Astier^{2,3}, M. Betoule^{2,3} and N. Regnault^{2,3}

¹Research School of Astronomy and Astrophysics, Australian National University, Canberra, ACT 2611, Australia

²ARC Centre of Excellence for All-sky Astrophysics (CAASTRO)

³Centre for Translational Data Science, University of Sydney, NSW 2006, Australia

⁴School of Physics and Astronomy, University of Southampton, Southampton, SO17 1BJ, UK

⁵Laboratoire de Physique Nucléaire et des Hautes Énergies, Université Pierre et Marie Curie Paris 6, Université Paris Diderot Paris 7, CNRS-IN2P3, 4 place Jussieu, 75252 Paris Cedex 05, France

⁶Email: rscalzo@anu.edu

(RECEIVED February 15, 2017; ACCEPTED June 16, 2017)

Abstract

The SkyMapper 1.3 m telescope at Siding Spring Observatory has now begun regular operations. Alongside the Southern Sky Survey, a comprehensive digital survey of the entire southern sky, SkyMapper will carry out a search for supernovae and other transients. The search strategy, covering a total footprint area of $\sim 2000 \text{ deg}^2$ with a cadence of $\leq 5 \text{ d}$, is optimised for discovery and follow-up of low-redshift type Ia supernovae to constrain cosmic expansion and peculiar velocities. We describe the search operations and infrastructure, including a parallelised software pipeline to discover variable objects in difference imaging; simulations of the performance of the survey over its lifetime; public access to discovered transients; and some first results from the Science Verification data.

Keywords: (cosmology:) dark energy – methods: data analysis – (stars:) supernovae: general

1 INTRODUCTION

The advent of automated, wide-field survey telescopes has revolutionised astronomy by dramatically increasing the sky area that can be observed to a given depth in a short span of time. At the same time, automation and digitisation of the end-to-end operation of these telescopes, including routine operation, data reduction, and data storage, has produced an unprecedented wealth of data to mine for new patterns and objects. The surveys employing these telescopes have created digital maps of large sky areas, such as the Sloan Digital Sky Survey (SDSS; York et al. 2000). They also enable increasingly intensive, untargeted monitoring of large sky areas for variable and transient objects. Such monitoring reduces the selection bias associated with targeting particular sky areas or host galaxies, and results in large, homogeneous samples of all transient phenomena in the sky in the targeted wavelength range to a certain magnitude limit. Completed time-domain surveys with a footprint larger than 1000 deg^2 include Palomar-QUEST (Djorgovski et al. 2008) and the Palomar Transient Factory (PTF; Rau et al. 2009; Law et al. 2009). Ongoing wide-area time-domain surveys include Pan-STARRS (Kaiser et al. 2010), LaSilla-QUEST (Baltay et al. 2013), the iPTF extension to PTF, and the Catalina Real-Time Transient Survey (CRTS; Drake et al. 2009).

A major science driver for time-domain surveys is the study of the Universe’s accelerating expansion (Riess et al. 1998; Schmidt et al. 1998; Perlmutter et al. 1999) and the parameters of the ‘dark energy’ that drives it, through the discovery and follow-up of type Ia supernovae (SNe Ia). Contemporary cosmological analyses such as the Joint Lightcurve Analysis (JLA; Betoule et al. 2014) require both high-redshift and low-redshift SNe Ia to make inferences about the dark energy equation of state; the low-redshift SNe Ia mainly constrain the mean absolute magnitude of SNe Ia, while the high-redshift SNe Ia use luminosity distances to map the Universe’s scale factor over cosmic time. Presently, the high-redshift SN Ia sample is composed of magnitude-limited surveys such as the Supernova Legacy Survey (SNLS; Sullivan et al. 2011; Conley et al. 2011) and the ongoing Dark Energy Survey (DES; Dark Energy Survey Collaboration 2016). Meanwhile, the current sample of low-redshift SNe Ia comes from a myriad of surveys through the 2000’s such as the Harvard-Smithsonian Center for Astrophysics (CfA) surveys (CfA1-4; Riess et al. 1999; Jha et al. 2006; Hicken et al. 2009, 2012) and the Carnegie Supernova Project (CSP; Contreras et al. 2010), which follow up SNe Ia discovered in the automated Lick Observatory Supernova Search (LOSS; Li et al. 2000; Filippenko et al. 2001) or by amateur astronomers. These SNe Ia

commonly were found by targeting large nearby galaxies. The accuracy and precision with which cosmological parameters can currently be measured from SNe Ia are limited by systematic errors, particularly photometric calibration (Betoule et al. 2013, 2014), but also including uncertainties in dust extinction (Phillips et al. 2013; Scolnic et al. 2014; Burns et al. 2014), potential population diversity (Quimby, Höflich, & Wheeler 2007; Wang et al. 2009; Kelly et al. 2010; Sullivan et al. 2010; Childress et al. 2013; Kelly et al. 2015), evolution (Kim et al. 2004; Howell et al. 2007; Sullivan et al. 2009; Milne et al. 2015) over a range of redshifts, or the influence of peculiar velocities (Davis et al. 2011) including coherent bulk flows (Hui & Greene 2006). Even the dust extinction in the Milky Way is subject to still unresolved systematics (e.g., Wolf 2014). Of the aforementioned systematics, the contributions to the uncertainty budget from photometric calibration and peculiar velocities are magnified by the heterogeneity of the low-redshift SN Ia sample, in particular by the numerous telescopes used to observe them, and by their non-uniform spatial distribution.

In March 2014, the SkyMapper robotic telescope (Keller et al. 2007) at Siding Spring Observatory commenced the SkyMapper Southern Sky Survey (SMSS),¹ an automated, digital survey of the southern sky. SkyMapper is a 1.3 m, $f/4.8$ telescope at Siding Spring Observatory, operated by the Australian National University on behalf of the Australian astronomical community. The telescope has a 5.7 deg^2 field of view, covering a square $2.4 \text{ deg} \times 2.4 \text{ deg}$ area with a fill factor of 91%. The 268-Mpix imager has a pixel scale of 0.5 arcsec/pix. Available filters include SDSS-like *griz*, Stromgren *u*, and a custom-made, intermediate-band *v* filter specific to SkyMapper (Bessell et al. 2011). The *v* filter covers the range 3670–3980 Å, to allow simultaneous measurements of surface gravity and metallicity from broad-band photometry; it is optimised to enable the SMSS’s key science goals in galactic archaeology, particularly the identification of extremely metal-poor stars (e.g. Keller et al. 2014; Howes et al. 2015). Further details about the SkyMapper instrument and its performance, the different observing programs falling under the SMSS and how they are scheduled, and the SMSS’s Science Data Pipeline (SDP) can be found in Wolf et al. (in preparation), which also describes the first SMSS data release.

Alongside the SMSS, the SkyMapper Transient Survey (SMT)² is a search for supernovae and transients in the local Universe optimised to discover and follow up SNe Ia for cosmology. SkyMapper aims to address the limitations of the current sample of nearby SNe Ia by searching a wide sky area uniformly with a short (≤ 5 d) cadence, in multiple well-determined bandpasses (Bessell et al. 2011). Thus, the resultant low-redshift ($z < 0.1$) SN Ia sample will be well calibrated and magnitude-limited, with a more similar selection function to the high- z sample. SMT will therefore be very

useful for measurements of cosmic expansion and peculiar velocities associated with bulk flows and cosmic structure, and for studies of the physics of SNe Ia aimed at improving SNe Ia as distance indicators. SkyMapper is also unique in its spatial overlap with the DES footprint, positioning SMT as an optimal low-redshift anchor.

Here, we introduce the infrastructure and operations of the SMT, and present some first results including performance during an early Science Verification period. SMT has begun operating at scale from April 2015, and has released candidates and classifications to the public. This paper will be followed shortly by an early data release of ~ 30 SNe Ia to date, and by individual papers on peculiar transients such as superluminous supernovae (Section 5.2). The structure of the paper is as follows: Section 2 gives an overview of SkyMapper telescope and the SMSS. Section 3 describes the search pipeline and follow-up procedure, while Section 4 focuses on survey strategy. We discuss and evaluate the performance thus far in Section 5, and present some early results in Section 6.

2 SKYMAPPER TRANSIENT SURVEY PIPELINE

Although SMT and SMSS both use the SkyMapper telescope, SMT has its own data reduction pipeline infrastructure, referred to as SUBPIPE below, maintained and run separately from the SMSS’s SDP. The two pipelines have different goals. The SDP is designed to ensure excellent absolute photometric calibration of non-transient sources. In contrast, SUBPIPE outsources much of the overhead for absolute calibration to the SDP, and focuses instead on rapid (< 12 h) turnaround for discovery of new transient candidates. To support transient science, SUBPIPE performs image subtraction (not done by the SDP) and provides additional data to support situational awareness of active transient candidates, such as historical light curves, a web service enabling follow-up of transients, and annotations by users about the transient type and characteristics. SUBPIPE is written almost entirely in Python, with some C++ extensions for pixel-level image processing (e.g. flat fielding) and incorporating commonly used open-source modules where available.

2.1 Image subtraction workflow

The structure of the SUBPIPE workflow is shown in Figure 1. Image subtraction requires a pre-existing template image of the sky (REF) to remove host galaxy light and non-variable sources from each new exposure (NEW). To obtain clean subtractions, the REF must be convolved by a suitably chosen kernel so that its point-spread function (PSF) matches that of the NEW. To use an image as a REF, we require that it has a narrower PSF than the NEW, and that it be taken at least two weeks prior to the NEW image (the rise time of a typical SN Ia to maximum light is about 17 d). If no REF image is available in a given part of the sky to subtract from a NEW

¹ <http://skymapper.anu.edu.au>

² <http://www.mso.anu.edu.au/skymapper/smt>

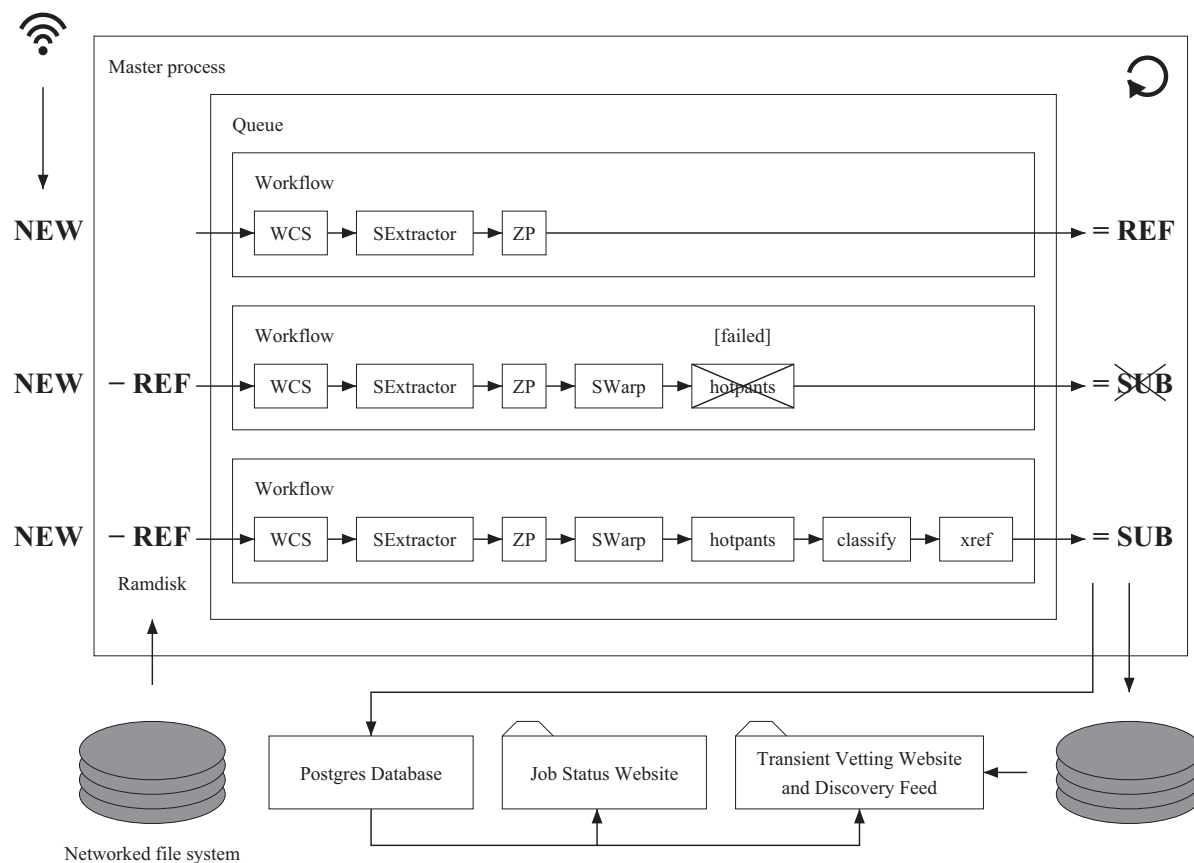


Figure 1. Architecture of SUBPIPE, the SMT pipeline.

image, the NEW image is simply added to the cache as a REF for future subtractions.

Reduction of an SMT exposure begins by splitting each SkyMapper mosaic image into individual 2048×4096 CCD images. An overscan region is subtracted from each half of the CCD (read out by separate amplifiers). Flat fields are constructed nightly from twilight flat images and applied to science exposures after overscan subtraction. A bad pixel map is created to flag pixels based on consistent deviation from a reasonable gain range and/or erratic behaviour. A quick large-scale astrometric solution for the mosaic is produced using ASTROMETRY.NET. If the astrometric registration fails (e.g. because of heavy cloud), or if the image quality is poor enough ($\text{FWHM} > 4$ arcsec, or elongation > 1.2) to severely impact the quality of subtractions and the false positive rate, the image is discarded at this stage and undergoes no further analysis; less than 5% of incoming images are lost to this cut. For each individual CCD of a NEW exposure, the workflow then proceeds through the following stages:

1. *WCS*: The world coordinate system for the NEW is refined, with higher order distortions described in the zenithal polynomial (ZPN) representation. This produces astrometry accurate to about 0.1 arcsec.

2. *SExtractor*: Sources are detected in the NEW image with SExtractor (Bertin & Arnouts 1996) and aperture photometry is extracted over a series of apertures (2, 3, 4, 5, 6, 8, and 10 arcsec in diameter).
3. *ZP*: A preliminary photometric zeropoint is produced by comparison to APASS (Henden & Munari 2014). Analysis of data from June 2014 suggests that the mean colour terms for transforming between the APASS and SkyMapper *ri* filters are small (< 0.05). SMT will eventually be tied to the same photometric system as the SMSS, pending completion of SMSS fields in the search area. If an image has no corresponding REF, it is added to the REF cache at this stage and no further processing takes place.
4. *SWarp*: The REF image is resampled to the coordinate system of the NEW image using SWARP (Bertin et al. 2002).
5. *hotpants*: The REF is scaled to the NEW flux level, convolved with a spatially varying kernel to match the NEW PSF as accurately as possible, and subtracted from the NEW using HOTPANTS³ to produce a subtracted image (SUB). Sources are detected in the SUB image with

³ <http://www.astro.washington.edu/users/becker/v2.0/hotpants.html>

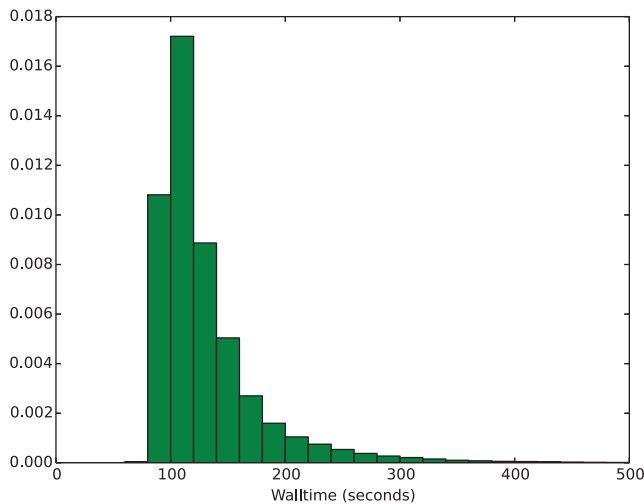


Figure 2. Distribution of processing times for successful subtraction jobs.

SEXTRACTOR. Each SUB image inherits the world coordinate system and photometric zeropoint of the corresponding NEW image.

6. *classify*: All detections on the SUB are run through an automated classification routine (see Section 2.3) to determine the likelihood that they are real astrophysical sources rather than artefacts from an imperfect subtraction process.
7. *xref*: All high-quality detections in the SUB image are astrometrically matched to previous detections. For sources passing a threshold number of high-quality detections in one or more subtractions, a historical light curve is compiled using all detections of the transient at that position.

Figure 2 shows the distribution of ‘wall times’ for the processing of a single SkyMapper CCD (running on a single core). The median processing time is 115 s from initial reduction to automatic flagging of candidates; with exposure times of 100 s in search images, which is fast enough to process an entire night’s worth of exposures in less than 24 h, allowing the pipeline to keep up with the flow of data. During Science Verification, we found that the end-to-end success rate for subtraction jobs was close to 99%, with a small number of failures easily traced to low-quality input data (due, for example, to poor weather conditions).

2.2 Image subtraction pipeline job control

The pipeline runs on a custom-built cluster named Maipenrai, hosted at the Australian National University’s Research School for Astronomy and Astrophysics (RSAA) in Canberra. The cluster has 48 cores with 192 GB of random-access memory and 44 TB of network-mounted disk space. A small part of the available memory (32 GB) is set aside as a fast virtual file system (ramdisk). This ensures that I/O-intensive processing by third-party image processing programs can be

performed directly in memory without modifying the code, dramatically improving performance. Relational information about images, pipeline jobs, and transient objects discovered is hosted in a Postgres database, accessed through the Django web framework.⁴ Commonly used catalogs, such as UCAC2 (Zacharias et al. 2000), 2MASS (Skrutskie et al. 2006), and APASS (Henden & Munari 2014), are accessed via a separate Postgres database hosted locally at RSAA. Figure 1 also shows a schematic representation of the flow control for the pipeline. To produce an architecture that is efficient, fault-tolerant, and transparent, we adhere to the following design principles:

1. A master process coordinates assignment of jobs to up to 32 worker processes at a time, monitoring their state through a polling loop. Each SkyMapper exposure is reduced using one worker process per 2048×4096 CCD, so that individual images fit easily in memory and no special software for reducing large mosaic images is needed.
2. Only the master process is allowed to transfer inputs and outputs of worker processes between shared disk and the ramdisk, which it does synchronously at the beginning and end of a polling cycle. This prevents many worker processes from accessing shared disk at once, placing minimal strain on networked file systems.
3. Although worker processes can query databases, the master process is responsible for updates to database tables, aggregating results from various processes to minimise I/O overhead.
4. The SMT footprint is organised around a set of fixed fields on the sky, corresponding to a subset of the SMSS fields. All shared disk storage is organised into subpaths corresponding to unique field/filter/CCD combinations.
5. Each worker process runs through a modular workflow, logging both the system calls needed to execute particular steps and the output of those steps to a log file. Any step which fails can be rerun easily based on the logged system calls, speeding up debugging. Process status and log files can be accessed quickly through a web interface.

2.3 Selecting candidates for photometric follow-up

The astrometric, photometric, and PSF matching of the REF to the NEW will in general not be perfect. Image subtraction artefacts not corresponding to astrophysical variable objects are easily recognisable to the human eye as anything in the SUB image not resembling a point source. However, these artefacts are much more numerous, outnumbering true astrophysical variable objects by more than an order of magnitude even in relatively clean subtractions. Initial triage of detected objects on subtractions must therefore be automated.

To address this challenge, we have implemented a series of machine learning classifiers to distinguish ‘Real’ astrophysical objects from ‘Bogus’ artefacts or cosmetic features

⁴ <https://djangoproject.com>

Table 1. Spectroscopically typed supernova discoveries during early SkyMapper operations.

Name	Disc. MJD (phase) ^a	RA	DEC	<i>z</i>	Type	ATel #
Science Verification (2013 Sep 04–2014 Mar 09)						
SMT J21413915–5643445	56573.6 (–8)	21:41:39.15	–56:43:44.5	0.142	Ia	5480
SMT J23032187–6911189	56592.6 (–3)	23:03:21.87	–69:11:18.9	0.060	Ia	5521 ^b
SMT J03054854–2850370	56626.6	03:05:48.54	–28:50:37.0	0.050	IIn	5622
SMT J03253351–5344190	56627.6 (–12)	03:25:33.51	–53:44:19.0	0.055	Ia	5641
SMT J00570507–3626231	56628.8 (+3)	00:57:05.07	–36:26:23.1	0.057	Ia	5620
SMT J03264288–3438055	56638.6 (+14)	03:26:42.88	–34:38:05.5	0.1	Ia	5602 ^c
SMT J03101002–3637448	56653.6 (+11)	03:10:10.02	–36:37:44.8	0.070	Ia	5650 ^d
SN 2013hx	56653.8	01:35:32.83	–57:57:50.6	0.130	SLSN	5912
SMT J04043173–6350154	56664.5 (+2)	04:04:31.73	–63:50:15.4	0.1	Ia	5748 ^e
SMT J05451320–4735425	56666.7 (–5)	05:45:13.20	–47:35:42.5	0.050	Ia	–
Zooniverse campaign (2015 Mar 12–22)						
SMT J10310056–3658262	57094.5 (+0)	10:31:00.56	–36:58:26.2	0.035	Ia	7261
SMT J13254308–2932269	57094.6	13:25:43.08	–29:32:26.9	0.040	Ic	7254
SMT J13545988–2820020	57094.6 (+0)	13:54:59.88	–28:20:02.0	0.038	Ia	7261
SMT J14323134–1339275	57095.7	14:32:31.34	–13:39:27.5	0.021	Ib	7261 ^f
SMT J13481313–3325189	57094.6 (+21)	13:48:13.13	–33:25:18.9	–	Ia	– ^g

^aPhase in days relative to *B*-band maximum light (type Ia only).

^bDiscovered independently and first confirmed as PSNJ23032177–6911185 by the CHASE survey.

^cDiscovered independently and first confirmed as LSQ13dbv.

^dDiscovered independently and first confirmed as LSQ13dkp.

^eDiscovered independently as OGLE-2014-SN-002.

^fDiscovered independently as LSQ15rw.

^gClassified by LCOGT as a Ia well after maximum light (G. Hosseinzadeh, private communication).

appearing in the search images. Our first version of this classifier used the Python-based machine learning package MILK⁵ to implement a random forest classifier modelled after Bloom et al. (2012). For more recent versions, we have switched to the random forest implementation in SKLEARN (Pedregosa et al. 2011), which trains more quickly and makes cross-validation easier.

At all stages of its development, the performance of the classifier has been limited mainly by the availability of training examples of Real events. The first version of the classifier used training data from early SkyMapper commissioning (August 2011), based on a sample of detections visually scanned and tagged as visually similar to Real or Bogus detections by human scanners. When evaluated against Real detections from contemporary data, this version of the classifier performs no better than random chance—possibly due to the lack of confirmed Real transients in the training set, and to the dramatic changes in the SkyMapper PSF from commissioning through to current operations. In May 2015, we retrained the classifier on a larger sample of Real detections of transients discovered by the pipeline (see Table 1), supplemented by a random selection of asteroids of varying magnitude as examples of Real objects visually resembling (hostless) transients in single exposures. A third version was trained in October 2016 using Real discoveries from the first year of full-time operations. As the number of Real transients increased, successive retrains have reduced our depen-

dence on non-transient detections tagged as Real, producing progressively more accurate results.

We evaluate the performance of all classifier models using *k*-fold cross-validation, in which the data are divided into *k* disjoint subsets, with *k* – 1 subsets reserved for training and the final subset used for validation. This technique enables most of the data to be used for training while determining the impact of certain subsets of data on classifier robustness. We chose *k* = 5 for our training. To make a fair estimate of the generalisation error from our small sample of Real transients, we placed multiple detections of the same transient in the same fold. This ensures that the training accounts for variations in observing conditions and transient magnitude, while the uncertainty in transient detection performance fairly reflects variations in host galaxy background and contrast, to which our classifier will be vulnerable when evaluating new detections. The total dataset for cross-validation includes 688 Real detections of 57 supernovae of all spectral types, 1 351 Real detections of asteroids, and 4 479 randomly selected Bogus detections.

We evaluate the classifier’s performance according to the efficiency (1.0 minus the missed detection rate) and purity (1.0 minus the false positive rate) of the classified candidates. Figure 3 shows the receiver operating characteristic (ROC) curve of these measures against each other, averaged over folds, demonstrating the trade-off resulting by varying the score threshold separating the Real and Bogus classes. The more recent classifier version is more efficient at high purity, with about 70% efficiency at 99% purity (somewhat worse than the Bloom et al. (2012) classifier on which it is

⁵ <https://github.com/luispedro/milk>

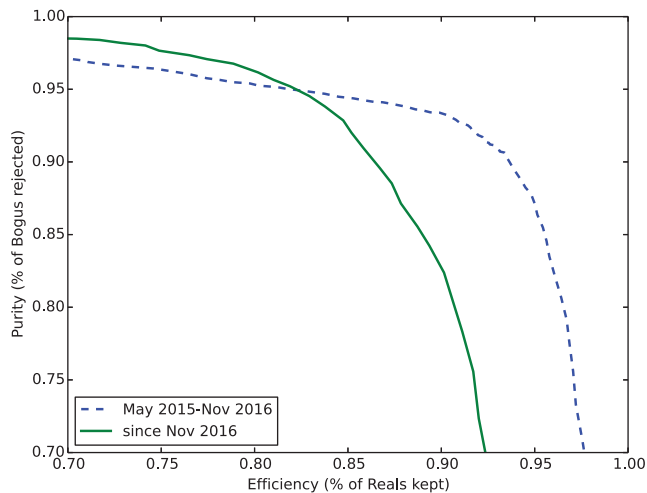


Figure 3. ROC curve (averaged among folds) for Real/Bogus classifier results.

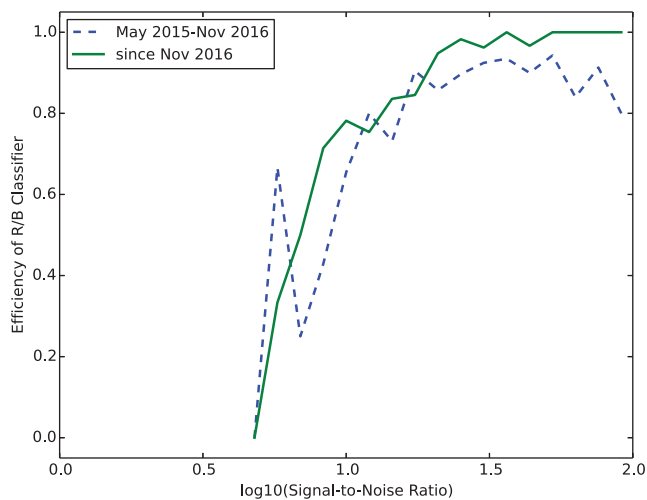


Figure 4. Classifier efficiency as a function of detection signal-to-noise.

based). [Figure 4](#) shows the efficiency of the more recent classifier version as a function of signal-to-noise ratio of the detection, demonstrating recent improvements in the effective signal-to-noise threshold and retention of bright detections. All versions of the classifier are archived and labelled so that the selection function for candidates can be reconstructed for later studies (e.g. SN Ia rates or SN Ia cosmology).

To further reduce the rate of false positives, we also require at least two Real detections of an object at the same location on separate nights or filters. Objects passing this cut are astrometrically matched to existing catalogs, including APASS (Henden & Munari 2014), the 2MASS Point Source Catalog (Skrutskie et al. 2006), and the SkyBot virtual observatory service for asteroids (Berthier et al. 2006). Any match better than 1 arcsec to the position of a known point source will cause the classification of that source to be carried over to the new candidate.

PASA, 34, e030 (2017)
doi:[10.1017/pasa.2017.24](https://doi.org/10.1017/pasa.2017.24)

Events with at least two detections (in any band) are passed on with annotations to astronomers to be reviewed for potential follow-up after every night of observing. The historical light curve is available for review, showing photometric detections and upper magnitude limits throughout the recent history of observations of each field. Each night, around 300 potential transients are sent to revision, only 10–20 are then scheduled for follow-up observations.

2.4 Follow-up

Once a candidate is selected for follow-up, it is placed in a queue for intensive monitoring by the SkyMapper telescope on a nominal 4-d cadence for *gri* (5-d for *v*), to ensure high-quality post-detection light curves.

Spectra for classification and scientific follow-up are taken as part of the ANU WiFeS SuperNova Program (AWSNAP; submitted to PASA), using the WiFeS integral field spectrograph (Dopita et al. 2007) on the RSAA 2.3-m telescope at Siding Spring Observatory, and as part of other spectroscopic surveys such as the Public ESO Spectroscopic Survey of Transient Objects (PESSTO; Smartt et al. 2014) and the Las Cumbres Observatory Global Telescope Network (Brown et al. 2013). These resources are in general 2–4-m class telescopes and suited for spectroscopic confirmation and follow-up of targets with peak $g < 19$, which for normal SNe Ia corresponds roughly to $z < 0.1$. Follow-up targets are shared with PESSTO via a live feed, and as of mid-2016 WiFeS observations take place in Target of Opportunity (ToO) mode. An API to report SMT transient candidates through the Transient Name Server⁶ is already implemented and working since December 2016. Transients reported can be also found in the SMT webpage.⁷

3 SURVEY STRATEGY AND SIMULATIONS

Here, we discuss the survey strategy for SMT, which serves to maximise the number of well-sampled SN Ia light curves that can be included in a cosmology sample.

3.1 Search and follow-up strategy

The SMT strategy is tuned to discover SNe Ia in the local universe, uniformly distributed in solid angle at high galactic latitudes ($b > 30$), and to produce high-quality multi-band light curves for cosmology. The strategy includes two components:

1. *Rolling search mode*: The telescope observes on a regular cadence (≤ 5 d) in the SkyMapper *gr* bandpasses. This mode does not explicitly target known galaxies, in order to produce a selection function as similar as possible to high-redshift SN Ia surveys such as SNLS.

⁶ <https://wis-tns.weizmann.ac.il/>

⁷ <http://www.mso.anu.edu.au/skymapper/smt/>

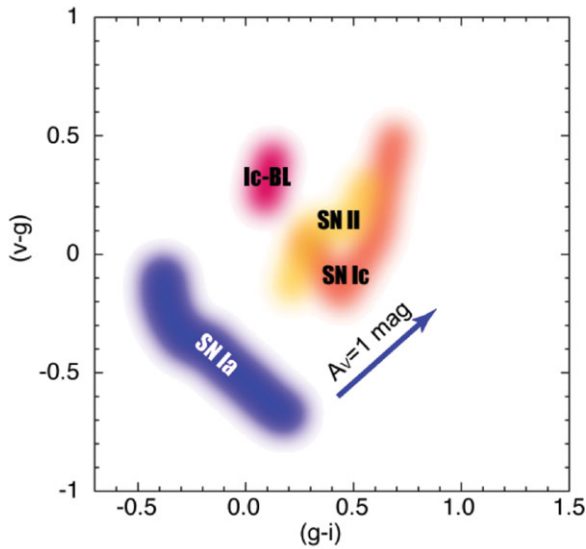


Figure 5. Subclasses of supernovae, including Type Ia and core-collapse (normal and broad-line Type Ic and Type II), at phases -10 to $+20$ d relative to peak, in a v - g - g - i colour-colour plot. This figure shows that v -band lightcurve points provide colour information for photometric selection of candidates to complement spectroscopic classification.

2. *Follow-up mode:* The telescope follows up fields with active transients using a tighter cadence with $vgri$ bandpasses (see Section 2.4). Although follow-up does not require SkyMapper’s wide field, it ensures that a uniform accurate calibration applies both to pre-discovery photometry from the rolling search and to the follow-up photometry. This mode also enables SMT to trigger on transients found in other public searches, to boost statistics and enable cross-calibration of SkyMapper photometry with photometry from other groups.

The exposure times for each bandpass are constrained by the desired limiting magnitude of our survey of $\sim 20.5 - 21$. The chosen exposure times are 100 s in g and r (for both search and follow-up), 300 s in i , and 500 s in v . Early SkyMapper v -band exposures are potentially valuable for photometric discrimination between SNe Ia and other types of supernovae (see Figure 5), and for examining the influence of progenitor metallicity on SN Ia luminosities. The v -band is read-noise dominated for exposures less than about 500 s long. We therefore include the *triggered follow-up* of 500 s v -band observations after the discovery of each SN Ia in our total observing time budget.

In order to optimise overall use of telescope time on SkyMapper, SMT uses the worst 30–35% of seeing conditions when in search mode, corresponding to a threshold seeing of >2.3 arcsec. These conditions are less useful for the SMSS, which prefer higher resolution images for greater depth and improved fine detail on extended objects such as galaxies. In contrast, SMT requires only the detection of point sources in relatively sparse fields, and the quality of

template subtractions remains reasonable for seeing better than 4 arcsec. This bad-seeing time is supplemented by time in any conditions (including good-seeing) so that SMT can maintain a semi-regular cadence on active fields in follow-up mode.

The number of fields covered by the footprint is constrained by the desired cadence, depth, and wavelength coverage, as well as the total amount of telescope time available to the survey. To better understand these trade-offs, we are carrying out additional simulations that take into account the characteristics of the instrument (throughput, PSF, read-out noise sky background for each filter) and historical variations in weather conditions at Siding Spring Observatory, including seeing and cloud cover. We report here on one such simulation of a baseline follow-up strategy as described above, in order to provide an indicative number of SNe Ia that might be found by SMT.

When using SNe Ia to constrain cosmological parameters, the distance modulus to any given SN Ia can be parametrised as

$$\mu = m_B + \alpha x_1 - \beta c - M_B, \quad (1)$$

where (m_B, x_1, c) are the parameters from a SALT2Guy et al. (2007, 2010) light curve fit, and α and β are standardisation parameters fit jointly with the cosmological parameters (Betoule et al. 2014, and references therein). The uncertainty σ_c in the colour c from the light curve fit is thus amplified by a factor $\beta \sim 3$ when calculating the distance modulus. We set a design ceiling of $\sigma_c < 0.03$ mag in order to keep its contribution to the distance modulus error distance modulus subdominant. The colour uncertainty as a function of cadence and instrument properties can be computed using a Fisher matrix analysis (Astier et al. 2011). Other factors, such as the accuracy of the underlying calibration of standard stars in the SkyMapper photometric system or the accuracy with which the SN Ia spectrophotometric sequence is modelled by a given light curve fitter, also influence the measured distance modulus, but these are extrinsic to data taken by SMT and so do not directly impact our choice of survey strategy.

The expected number N of SNe Ia to be found in the survey can be estimated by Monte Carlo, integrating

$$N = \int d\Omega \int dt \int dz \frac{\partial V}{\partial z} \eta(z, \Omega, t) \quad (2)$$

over time t , the survey footprint Ω , and redshift z ; here dV is the co-moving volume element at redshift z , and η is the survey efficiency for discovery of SNe Ia including the particulars of the timing and depth of each image relative to a randomly generated set of SN Ia light curves. We estimate an effective significance threshold of 9σ for single-epoch detections based on the empirical Real/Bogus classifier efficiency curve (Figure 4), and require two gr detections above this threshold at two separate epochs in order to detect a SN Ia and flag it as a candidate.

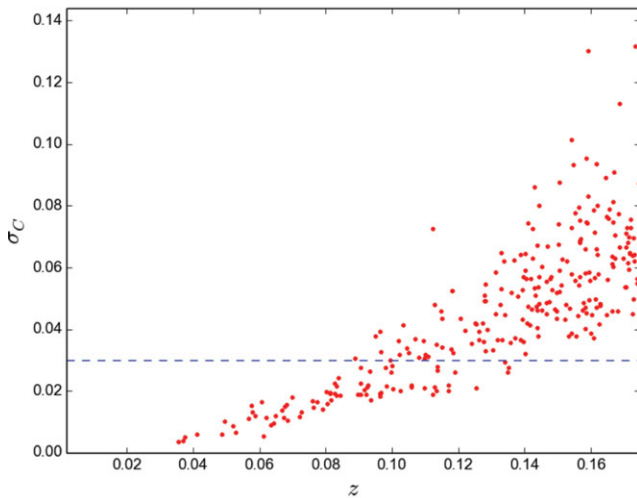


Figure 6. Uncertainty in colour determination for a suite of light curve realisations from a simulation of six months of a SkyMapper cosmology survey. The colour uncertainty σ_c represents the formal statistical error in the light curve fit, taking into account the effects of seeing and weather (sampled from Siding Spring Observatory weather logs) on the achieved image depth and cadence.

Based on the chosen exposure times and a nominal 4-d follow-up cadence, and taking readout and slewing overheads into account, SMT can usefully monitor about 150 fields at a time. Monte Carlo integration of Equation (2) suggests that we can discover about 100 SNe Ia per year with $z < 0.1$ that have light curves with $\sigma_c < 0.03$ mag—a reasonably large contribution of well-calibrated SNe Ia to the nearby cosmology sample. A scatter plot of σ_c versus redshift for one realisation of a 6-month survey period is shown in Figure 6.

3.2 Survey geometry

Coherent peculiar motions in the local Universe produce spatially correlated deviations in peculiar velocities from a uniform Hubble flow; accurate constraints on bulk flows require coverage over a large area on the celestial sphere (Hui & Greene 2006). Unless the entire sky is covered uniformly, survey geometry may affect the final performance of the survey. Haugbølle et al. (2007) argued that accurate measurements of peculiar velocities required a survey geometry that minimised the size of holes in the footprint. The large dust extinction in the plane of the Galaxy constrains the survey geometry, since Milky Way dust is the second-largest source of systematic uncertainty in SN Ia distances (after photometric calibration) in contemporary SN Ia Hubble diagrams (Conley et al. 2011; Betoule et al. 2014). The Schlafly & Finkbeiner (2011) recalibration of the Schlegel et al. (1998) dust maps represent an improvement, although residuals at the 10–30 mmag level still exist even for objects at low reddening (Wolf 2014).

The influence of different survey geometries on bulk flow constraints for SMT has been simulated in Scrimgeour et al.

(in preparation) including random sets of fields selected uniformly in area, ‘glass’ geometries meant to minimise holes in coverage, and geometries avoiding the Galactic plane (with a maximum Milky Way extinction or minimum Galactic latitude). They found that the total number of SNe Ia discovered and the combination of the SkyMapper SN Ia sample with northern-hemisphere samples (such as PTF) were each more influential factors than the choice of any specific survey geometry. Therefore, it makes sense for SMT to choose fields to minimise Galactic extinction, although new fields may be added as the survey progresses, in order to improve constraints on the bulk flow.

SMT will therefore concentrate on a set of low-extinction fields ($E(B - V)_{\text{MW}} < 0.05$). This strategy will ensure the pre-existence of deep galaxy references, which dramatically increase the expected SN Ia yield in our simulations (by nearly a factor of 2) relative to the Science Verification case where galaxy reference images are comparable in depth to the search images.

Additionally, we are following areas of the sky currently prioritised for SMSS coverage by other extra-galactic programs, including the Shapley Supercluster and the footprint of the Kepler Extra-Galactic Survey (KEGS), which is using the Kepler K2 mission to monitor supernova fields at a very high-cadence of 30 min (see Figure 7). K2 fields 1, 3, 4, 5, 6, 8, 10, 12, 14, 16, and 17 have been KEGS focused fields, discovering to date 23 supernovae of all types, several of which been observed by SkyMapper (Rest et al. in preparation; Tucker et al. in preparation; Zenteno et al. in preparation).

4 SURVEY PERFORMANCE

In this section, we summarise the data taken for SMT, and evaluate its performance based on expectations from detailed simulations of the survey history.

4.1 Early survey

SkyMapper’s performance has evolved over the commissioning period. Early SkyMapper images were limited in quality by vibrations at ~ 30 Hz driven by a resonance with the cooling system for the camera; these were mitigated by modifications to change the telescope’s resonant frequency. During the Science Verification period for SMT (2013 September 04 to 2014 March 09), the median image quality was ~ 3.5 arcsec. After March 2014, additional improvements to focus and tracking resulted in a median image quality near 2 arcsec in *gri* bands. The readout overhead has also decreased, from a mean of 45 s during Science Verification to 21 s as of April 2014.

From April 2014 to April 2015, the SkyMapper telescope was dedicated to an intensive full-sky observing campaign for the SMSS (Wolf et al., in preparation). SMT observing did not resume until April 2015.

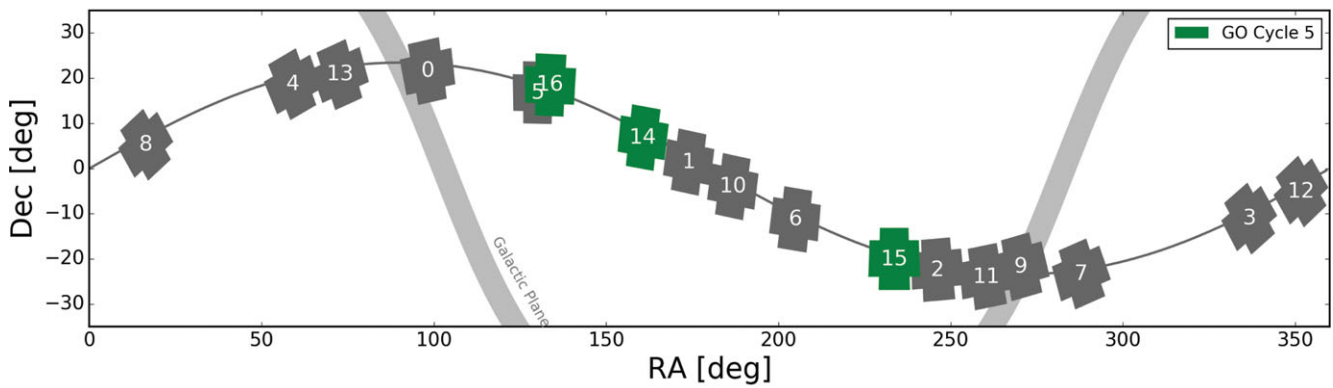


Figure 7. Figure courtesy of the NASA Kepler Guest Observer office. These are the footprints for the K2 campaigns, which lie along the ecliptic, with the green fields to be observed by both SkyMapper and Kepler in 2017. The Kepler Extra-Galactic Survey is monitoring, and SkyMapper is shadowing with ground-based multi-colour observations, supernovae in Campaigns 1, 3, 4, 5, 6, 8, 10, 12, 14, and 16. Kepler fields listed were partially observed, with limitations based on field orientation and visibility. Field 16 will be a forward-facing field with the entire field visible from the ground in its entirety.

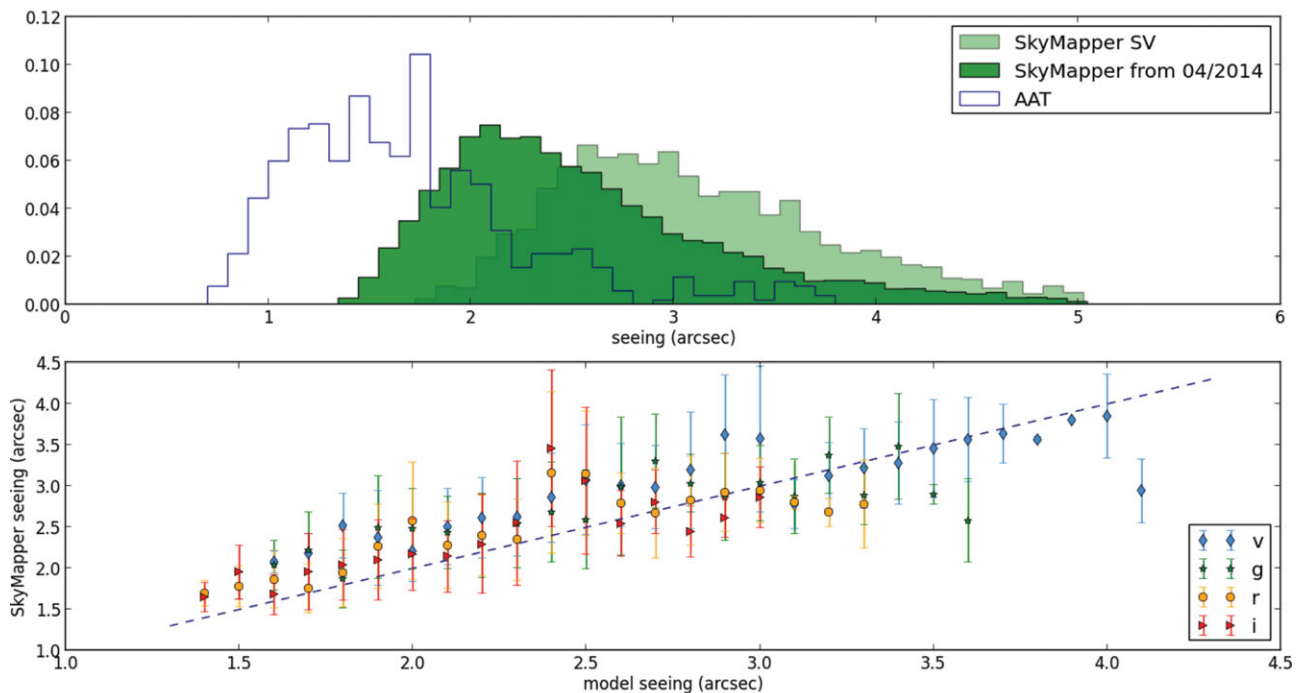


Figure 8. Top: Histograms of *g*-band seeing for the SkyMapper telescope during Science Verification (light green) and after additional hardware intervention completed April 2014 (dark green), as compared to AAT seeing logs (open). Bottom: SkyMapper seeing in *vgri* bands from April 2014 to May 2015, compared with predictions from the transfer function.

4.2 Image quality

Figure 8 shows the distribution of SkyMapper seeing in a representative filter (*g*), in comparison to the distribution obtained from weather logs at the Anglo-Australian Telescope (AAT) assumed to be the natural seeing of the Siding Spring site. To assist us in running simulations to determine the performance of our survey over a long historical period using past weather logs, we developed a transfer function to predict SkyMapper seeing from weather log entries. The model takes into account nightly variations in seeing (measured at the AAT), wavelength dependence, and airmass: for a filter

with effective wavelength λ and seeing s_λ ,

$$s_\lambda^2 = s_{SM,0}^2 + \left[s_{AAT}^{1+\alpha} X^\gamma \left(\frac{\lambda}{5500\text{\AA}} \right)^\beta \right]^2, \quad (3)$$

where $s_{SM,0} = 1.1$ arcsec is a baseline seeing floor, and α , β , and γ are coefficients characterising atmospheric scattering. For contemporary data (taken after April 2014), chi-square minimisation produces best-fit values $\alpha = -0.156$, $\beta = -0.5$, $\gamma = 0.8$.

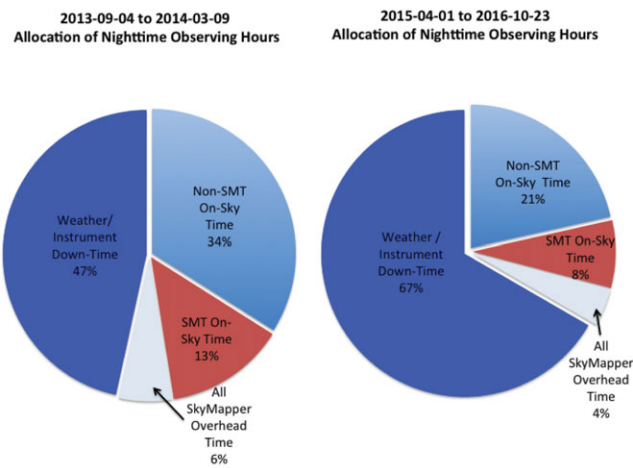


Figure 9. Impact of weather on SMSS and SMT operations as of 2016 October 23.

4.3 Delays and limitations

Through 2015 to early 2016, the SkyMapper telescope experienced various technical difficulties which delayed progress. In particular, two lengthy repairs on the cooling system halted SkyMapper observations for nearly 4 months in total, from 2015 September 24 to 2015 November 24 and again from 2016 January 04 to 2016 February 26. Long periods of inclement weather (see Figure 9) during the winter have frustrated the search for transients, with both SkyMapper and the 2.3-m telescope often being closed. This has adversely affected light curve quality and sampling, with numerous promising candidates fading before classification was possible, and/or left with large gaps in the light-curve.

As more of the SMSS footprint (Figure 10) is completed, more SMT fields will have deep references. This will decrease the time cost of building REF images during SMT time, compared to the early survey. The search has operated continuously from April 2016, during which transients have steadily been discovered and classified.

5 FIRST RESULTS

5.1 First discoveries: Science Verification and the Zooniverse

Table 1 reports the types and numbers of confirmed supernovae discovered (see Figure 11 for colour composite images) during early SkyMapper operations. During Science Verification, the Search produced 10 spectroscopically confirmed supernovae, among them 8 SNe Ia.

Supernova observations resumed during the period 2015 March 12–20, during which SkyMapper performed an intensive observing campaign with a short cadence of 1–2 d, as an outreach effort in partnership with the Zooniverse citi-

zen science community. An additional five spectroscopically confirmed supernovae were discovered in this campaign, including three SNe Ia. Thumbnails of candidates found in the search appeared on the Zooniverse website as the ‘Snapshot Supernova’ project, and were processed by volunteers using the decision tree described in Smith et al. (2011). Popular candidates were inspected by the authors and submitted in real time for spectroscopic classification by the PESSTO collaboration using the ESO NTT 3.6-m telescope at La Silla.

An example of typical light curve quality in the early survey is shown in Figure 12 for SMTJ10310056–3658262, a SN Ia discovered during the Zooniverse campaign. We find that the quick photometry used in our search is precise to about 0.03 mag, already good enough for most non-SN Ia science and presenting no barrier to discovery and selection for follow-up. Upcoming data releases of SN Ia light curves will improve upon this by reprocessing photometry for the released targets only.

Figure 10 shows a map of the total SMT coverage to date. A total of 393 SkyMapper fields, or $2\,250\text{ deg}^2$, have been observed, with a mean of 40 visits since the beginning of Science Verification.

We use the historical cadences and upper limits from successful subtractions to perform Monte Carlo simulations of SNe Ia as discovered by the historical survey in the period April–November 2016, when the instrument configuration was stable and the survey was working well. We use the same effective detection threshold of 9σ to represent the classifier efficiency as in our cosmology simulations from Section 3.1. Based on these simulations, we expect a total of 65 ± 8 SNe Ia to be detected by the survey during April–November 2016, assuming two significant detections on separate nights in any filter were necessary for detection. If instead simultaneous detections in both g and r are required, we expect 41 ± 6 SNe Ia instead. Of these, we expect 13 ± 3 SNe Ia to peak at $g < 19$, and therefore to be recommended for spectroscopic confirmation.

Our actual survey operations confirmed 13 SNe Ia during this period; an additional 39 transient objects with Ia-like light curve timescales and colours were discovered, but had no spectra taken either because they were too faint or were discovered past maximum light. These numbers are in good agreement with the expectations from our simulations. The simulations are approximate and do not take into account other effects at the pixel level as a more sophisticated treatment appropriate for a SN Ia rates measurement would do; these might include pixel-level simulations of classifier efficiency or observational bias against SNe Ia on the cores of bright host galaxies (which one might expect to be worse for a bad-seeing search relative to one done in better seeing). However, the numbers of SNe Ia discovered by our survey so far appear to be in good agreement with the simulations, suggesting that our selection effects are well understood and that our estimate of SMT’s potential for future SN Ia discoveries is reasonable.

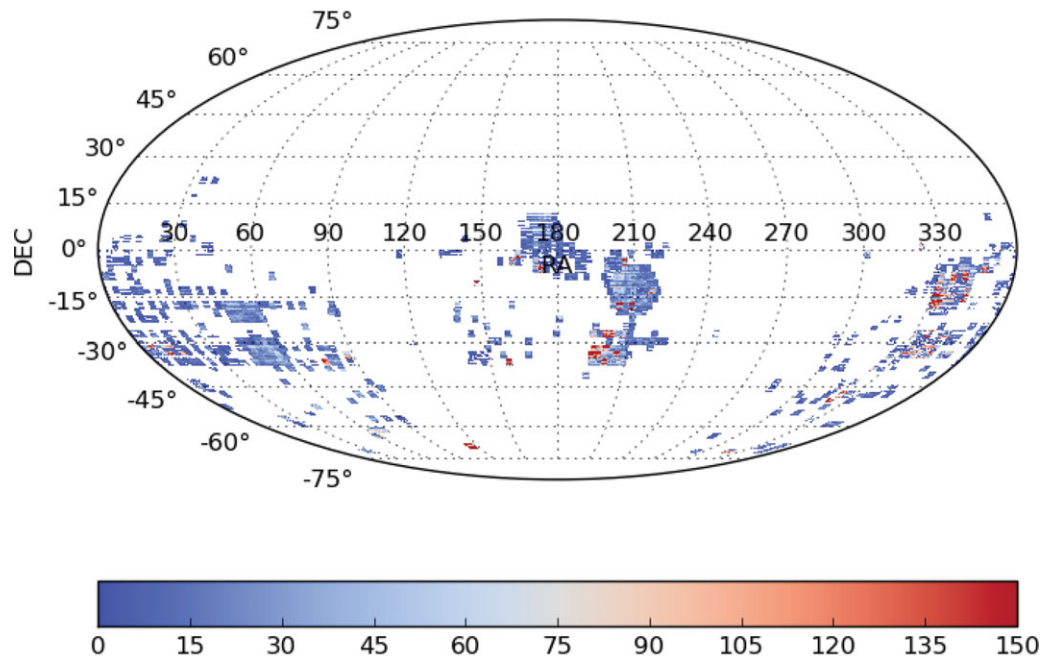


Figure 10. Map of SMT sky coverage, shown as a heat map in which the colour bar represents the cumulative number of visits of SMT to each SkyMapper field as of 2016 October 20. White areas have no coverage, whereas coloured regions indicate that the area has been observed at least once.

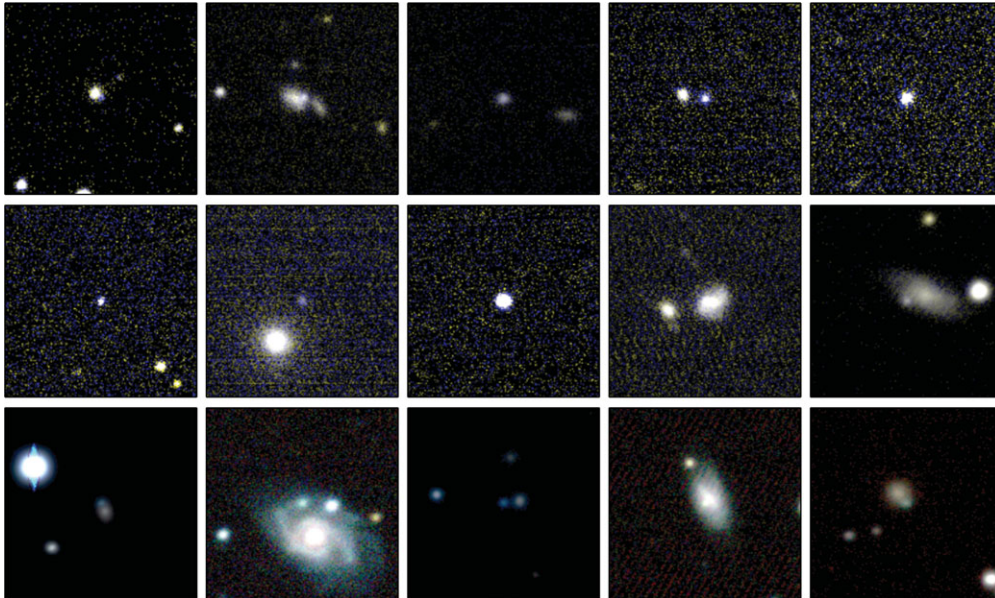


Figure 11. Colour composite thumbnail images of the supernovae from Table 1. The images shown are NEW images, with each supernova centred in the figure.

5.2 Unique peculiar objects

In addition to SNe Ia, SMT is discovering other types of supernovae and stellar transients, such as superluminous supernovae (Quimby et al. 2011; Gal-Yam 2012) and faint calcium-rich transients (Kasliwal et al. 2012), which occur preferentially in low-surface-brightness, star-forming host galaxies or on the outskirts of larger galaxies not monitored by tar-

geted searches (Yuan et al. 2013). Although the SMT search cadence is optimised for normal SNe Ia, we devote a small fraction (5–10%) of our follow-up resources to individual objects of interest that are likely to generate high-impact single-object papers.

The first notable exotic transient event discovered by SMT was SN 2013hx (discovered as SMT J013533283–5757506), a superluminous supernova initially similar to SN 2010gx

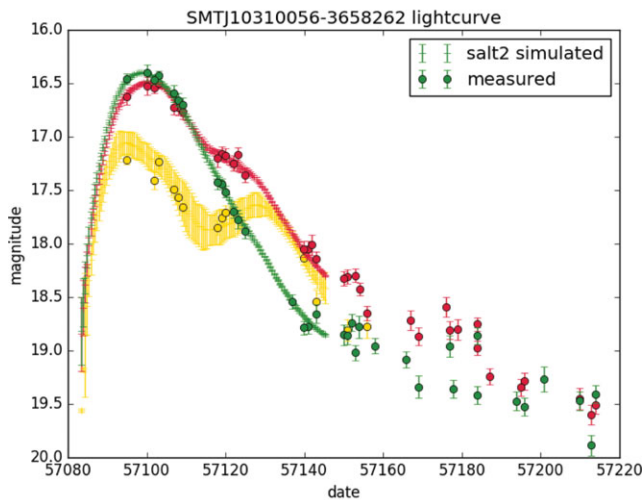


Figure 12. Lightcurve and SALT2 fit of SMTJ10310056–3658262, discovered during the Zooniverse campaign, in *gri* colours. The squares show observed photometry points, and the error bars represent the model lightcurves using the SALT2 fit (over the phase range allowed by the SALT2 model).

(Pastorello et al. 2010) but displaying broad $H\alpha$ emission at late times (Inserra et al. 2016). SN 2013hx was discovered by SkyMapper at MJD 56657.6 (2013 December 31 UT), and reached peak magnitudes $g = 16.9$, $r = 17.0$ at MJD 56683.5 (2014 January 26 UT). At a redshift of 0.130, SN 2013hx was the closest superluminous type II supernova discovered to date (Nicholl et al. 2014), presenting an excellent opportunity for late-time observations. SN 2013hx was also included in a recent study of superluminous supernova light curves (Nicholl et al. 2015). Other exotic transients discovered so far include SN 2015J, a possible supernova impostor or magnetar-powered type Ic supernova (Tucker et al. in preparation), and an object similar to Arcavi et al. (2016) in the so-called superluminous-gap (Zhang et al. in preparation). We may also be sensitive to shock interaction with SN Ia companions, as observed in SN 2016hhd (Möller et al. in preparation).

6 SUMMARY

This work presents the SkyMapper Transient Survey, including the software specific to the search for transients and the planned survey strategy. The software involves a sophisticated image subtraction pipeline with a machine learning classifier and a web admin interface for human input. We describe the early performance of the Survey, which is steadily assembling a small sample of SNe Ia for inclusion in a low-redshift cosmology sample (to be detailed in a forthcoming data release paper), and in addition discovering peculiar objects interesting in their own right (Tucker et al. in preparation; Zhang et al. in preparation; Möller et al. in preparation).

PASA, 34, e030 (2017)
doi:10.1017/pasa.2017.24

ACKNOWLEDGEMENTS

Parts of this research were conducted by the Australian Research Council Centre of Excellence for All-sky Astrophysics (CAASTRO), through project number CE110001020. RS and CW acknowledge support from ARC Laureate Grant FL0992131. This research was made possible through the use of the AAVSO Photometric All-sky Survey (APASS), funded by the Robert Martin Ayers Sciences Fund. We thank Geert Barensten and the Kepler Guest Observer Office for their assistance in constructing Figure 7. We gratefully acknowledge the assistance of over 40 000 online volunteers for the Snapshot Supernova program in March 2015, run in partnership with the Zooniverse citizen science portal. We also thank Andy Howell and the LCOGT team for providing us with a spectroscopic classification for SMT J13481313–3325189. We acknowledge and thank PhD students: F. Panther, R. Ridden-Harper, and N.E. Sommer as well contributions by summer students: P. Armstrong, G. Taylor, E. Moore, C. Bray, and Y. Chen.

REFERENCES

- Arcavi, I., et al. 2016, *ApJ*, **819**, 35
Astier, P., Guy, J., Pain, R., & Balland, C. 2011, *A&A*, **525**, A7
Baltay, C., et al. 2013, *PASP*, **125**, 683
Berthier, J., Vachier, F., Thuillot, W., Fernique, P., Ochsenbein, F., Genova, F., Lainey, V., & Arlot, J.-E. 2006, in ASP Conf. Ser. Vol. 351, *Astronomical Data Analysis Software and Systems XV*, eds. C. Gabriel, C. Arviset, D. Ponz, & S. Enrique (San Francisco: ASP), 367
Bertin, E., & Arnouts, S. 1996, *A&AS*, **117**, 393
Bertin, E., Mellier, Y., Radovich, M., Missonnier, G., Didelon, P., & Morin, B. 2002, in ASP Conf. Ser. Vol. 281, *Astronomical Data Analysis Software and Systems XI*, eds. D. A. Bohlender, D. Durand, & T. H. Handley (San Francisco: ASP), 228
Bessell, M., Bloxham, G., Schmidt, B., Keller, S., Tisserand, P., & Francis, P. 2011, *PASP*, **123**, 789
Betoule, M., et al. 2013, *A&A*, **552**, A124
Betoule, M., et al. 2014, *A&A*, **568**, A22
Bloom, J. S., et al. 2012, *PASP*, **124**, 1175
Brown, T. M., et al. 2013, *PASP*, **125**, 1031
Burns, C. R., et al. 2014, *ApJ*, **789**, 32
Childress, M., et al. 2013, *ApJ*, **770**, 108
Conley, A., et al. 2011, *ApJS*, **192**, 1
Contreras, C., et al. 2010, *AJ*, **139**, 519
Dark Energy Survey Collaboration et al. 2016, *MNRAS*, **460**, 1270
Davis, T. M., et al. 2011, *ApJ*, **741**, 67
Djorgovski, S. G., et al. 2008, *AN*, **329**, 263
Dopita, M., Hart, J., McGregor, P., Oates, P., Bloxham, G., & Jones, D. 2007, *Ap&SS*, **310**, 255
Drake, A. J., et al. 2009, *ApJ*, **696**, 870
Filippenko, A. V., Li, W. D., Treffers, R. R., & Modjaz, M. 2001, in ASP Conf. Ser. Vol. 246, *IAU Colloq. 183: Small Telescope Astronomy on Global Scales*, eds. B. Paczynski, W.-P. Chen, & C. Lemme (San Francisco: ASP), 121
Gal-Yam, A. 2012, *Sci*, **337**, 927
Guy, J., et al. 2007, *A&A*, **466**, 11
Guy, J., et al. 2010, *A&A*, **523**, A7
Haugbølle, T., Hannestad, S., Thomsen, B., Fynbo, J., Sollerman, J., & Jha, S. 2007, *ApJ*, **661**, 650
Henden, A., & Munari, U. 2014, *CoSka*, **43**, 518
Hicken, M., et al. 2009, *ApJ*, **700**, 331

- Hicken, M., et al. 2012, *ApJS*, **200**, 12
- Howell, D. A., Sullivan, M., Conley, A., & Carlberg, R. 2007, *ApJL*, **667**, L37
- Howes, L. M., Casey, A. R., Asplund, M., et al. 2015, *Nature*, 527, 484
- Hui, L., & Greene, P. B. 2006, *PhRvD*, **73**, 123526
- Inserra, C., et al. 2016, arXiv:1604.01226
- Jha, S., et al. 2006, *AJ*, **131**, 527
- Kaiser, N., et al. 2010, in *SPIE Conf. Ser. Vol. 7753, Ground-Based and Airborne Telescopes III*, eds. L. M. Stepp, R. Gilmozzi, & H. J. Hall (Bellingham: SPIE), 77330E
- Kasliwal, M. M., et al. 2012, *ApJ*, **755**, 161
- Keller, S. C., et al. 2007, *PASA*, **24**, 1
- Keller, S. C., et al. 2014, *Nature*, **506**, 463
- Kelly, P. L., Hicken, M., Burke, D. L., Mandel, K. S., & Kirshner, R. P. 2010, *ApJ*, **715**, 743
- Kelly, P. L., Filippenko, A. V., Burke, D. L., Hicken, M., Ganeshalingam, M., & Zheng, W. 2015, *Sci*, **347**, 1459
- Kim, A. G., Linder, E. V., Miquel, R., & Mostek, N. 2004, *MNRAS*, **347**, 909
- Law, N. M., et al. 2009, *PASP*, **121**, 1395
- Li, W. D., et al. 2000, in *AIP Conf. Ser. Vol. 522, Cosmic Explosions: Tenth Astrophysics Conference*, eds. S. S. Holt & W. W. Zhang (Melville: AIP), 103
- Milne, P. A., Foley, R. J., Brown, P. J., & Narayan, G. 2015, *ApJ*, **803**, 20
- Nicholl, M., et al. 2014, *MNRAS*, **444**, 2096
- Nicholl, M., et al. 2015, *MNRAS*, 452, 3869
- Pastorello, A., et al. 2010, *ApJL*, **724**, L16
- Pedregosa, F., et al. 2011, *JMLR*, **12**, 2825
- Perlmutter, S., et al. 1999, *ApJ*, **517**, 565
- Phillips, M. M., et al. 2013, *ApJ*, **779**, 38
- Quimby, R., Höflich, P., & Wheeler, J. C. 2007, *ApJ*, **666**, 1083
- Quimby, R. M., et al. 2011, *Nature*, **474**, 487
- Rau, A., et al. 2009, *PASP*, **121**, 1334
- Riess, A. G., et al. 1998, *AJ*, **116**, 1009
- Riess, A. G., et al. 1999, *AJ*, **117**, 707
- Schlafly, E. F., & Finkbeiner, D. P. 2011, *ApJ*, **737**, 103
- Schlegel, D. J., Finkbeiner, D. P., & Davis, M. 1998, *ApJ*, **500**, 525
- Schmidt, B. P., et al. 1998, *ApJ*, **507**, 46
- Scolnic, D. M., Riess, A. G., Foley, R. J., Rest, A., Rodney, S. A., Brout, D. J., & Jones, D. O. 2014, *ApJ*, **780**, 37
- Skrutskie, M. F., et al. 2006, *AJ*, **131**, 1163
- Smartt, S. J., et al. 2015, *A&A*, **579**, 40
- Smith, A. M., et al. 2011, *MNRAS*, **412**, 1309
- Sullivan, M., Ellis, R. S., Howell, D. A., Riess, A., Nugent, P. E., & Gal-Yam, A. 2009, *ApJL*, **693**, L76
- Sullivan, M., et al. 2010, *MNRAS*, **406**, 782
- Sullivan, M., et al. 2011, *ApJ*, **737**, 102
- Wang, X., et al. 2009, *ApJL*, **699**, L139
- Wolf, C. 2014, *MNRAS*, **445**, 4252
- York, D. G., et al. 2000, *AJ*, **120**, 1579
- Yuan, F., Kobayashi, C., Schmidt, B. P., Podsiadlowski, P., Sim, S. A., & Scalzo, R. A. 2013, *MNRAS*, **432**, 1680
- Zacharias, N., et al. 2000, *AJ*, **120**, 2131